Advances in Water Resources 185 (2024) 104659

Contents lists available at ScienceDirect

Advances in Water Resources

journal homepage: www.elsevier.com/locate/advwatres

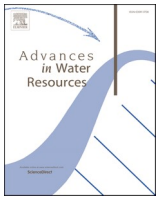

Unraveling residual trapping for geologic hydrogen storage and production using pore-scale modeling

Siqin Yu [a,b], Mengsu Hu [a,*], Carl I. Steefel [a], Ilenia Battiato [b]

[a] Energy Geosciences Division, Lawrence Berkeley National Laboratory, Berkeley, CA, USA
[b] Department of Energy Science and Engineering, Stanford University, Stanford, CA, USA

ARTICLE INFO

Keywords:
Residual trapping
Underground hydrogen storage
Cyclic injection and withdrawal
Geologic hydrogen production
Pore-scale modeling

ABSTRACT

Residual trapping is an important process that affects the efficiency of cyclic storage and withdrawal and *in-situ* production of hydrogen in geological media. In this study, we have conducted pore-scale modeling to investigate the effects of pore geometry and injection rate on the occurrence and efficiency of residual trapping via dead-end bypassing. We begin our theoretical and numerical analyses using a single rectangular pore to understand the key controls in bypassing. We further investigated two factors affecting bypassing: (a) a continuous cycle of injection-extraction of H_2, and (b) variable pore geometry. Based on our pore-scale simulations, we found that: (a) a higher pore height/width ratio (h/w) and a higher injection rate cause more residual trapping, which is unfavorable for withdrawal of H_2; (b) the trapping percentage increases with the h/w first and then decreases after h/w reaches 0.5; (c) and a converging-shaped pore can result in less trapping volume. Based on a theoretical comparison of the residual trapping behavior of H_2 and CO_2, we discuss the mechanisms that are applicable to CO_2 residual trapping and the possibility of developing engineering controls of H_2 storage and production.

Plain language summary

Residual trapping is an important trapping mechanism that needs to be accounted for in geologic hydrogen storage and production. Laboratory research has been conducted previously at the core scale that gave insight and qualitative understanding, but a quantitative analysis at the scale of pore has never been attempted. In this study, we conducted pore-scale modeling of hydrogen to investigate the effects of pore geometry and injection rate on residual trapping via dead-end bypassing. We began with a rectangular pore and added complexity in terms of an injection-withdrawal cycle and varied geometry. Our results show that the pore geometry (e.g., height/width ratio, h/w, the shape of the pore) along with injection rate affects the trapping percentage, and this may be controlled by engineering operations. Considering the similarity between H_2 and CO_2, the mechanisms that were found on H_2 residual trapping may also be applicable to geological CO_2 storage.

1. Introduction

Hydrogen is a low-carbon energy carrier that offers a promising energy storage solution and can limit global climate change by reducing carbon emissions. Because H_2 can be stored, combusted, and combined in chemical reactions like natural gas, oil, and coal, it represents an important option for reducing carbon emissions (Birol, 2019). Geological storage of H_2 offers megawatt-to-gigawatt power storage capacity and the possibility for extended discharge times (Wallace et al., 2021).

Salt caverns are among the important geological settings that have been used to store H_2 or mixed gases. Taking advantage of the low permeability of natural salt rocks and the well-confined space within salt caverns, cyclic injection and withdrawal of H_2 can be accomplished because of its relatively easy flow and confinement. However, the relatively limited distribution of salt rocks in the world, the potential significant reduction of the storage space because of the creep behavior of salt rocks (National research council, 1996; Hu et al., 2021), the potential fracturing/damage of salt rocks (Tounsi et al., 2023), and the potential leakage makes it questionable whether they are viable for

* Corresponding author.
E-mail address: mengsuhu@lbl.gov (M. Hu).

https://doi.org/10.1016/j.advwatres.2024.104659
Received 9 November 2023; Received in revised form 25 January 2024; Accepted 13 February 2024
Available online 14 February 2024

large-scale H_2 storage.

An alternative promising geological media for H_2 storage are porous medium formations given their capacity and accessibility. These include depleted oil and gas shale and sandstone reservoirs, and deep saline aquifers (Heinemann et al., 2021; Hassanpouryouzband et al., 2021). With the larger volumes of porous media available, storage of H_2 in the subsurface seems to be straightforward. However, H_2 is a very low density gas. This makes retrieval of H_2 that has been stored in an unconfined porous reservoir very challenging. Also importantly, H_2 in porous formations can involve geochemical reactions and microbial activity, which can potentially lead to H_2 loss (Dopffel et al., 2023), gas contamination (Hassannayebi et al., 2019), wettability change (Liu et al., 2023) and bioclogging effects (Eddaoui et al., 2021). Experimental studies suggest a significant pH increase under high-saline-conditions and wettability change when microbes make use of hydrogen as an electron donor . Moreover, new investigations were conducted on H_2/brine displacement behavior at both pore scale (van Rooijen et al., 2022; Lysyy et al., 2023; Liu et al., 2023; Jangda et al., 2023; Hashemi et al., 2021) and core scale (Boon and Hajibeygi, 2022; Thaysen et al., 2023; Wang et al., 2023). These recent experimental observations suggest different dynamic behavior for H_2 compared with CO_2 because of the unique physical properties of H_2. Overall, to make geological storage of H_2 in porous media a globally viable solution, it is important to understand how H_2 flows in porous sediments and rocks, and how H_2 and its flow and trapping are influenced by the rocks, minerals, and microbes present in the reservoirs.

Meanwhile, geologic hydrogen has emerged as a promising new clean energy source (Hand, 2023). One approach to generating hydrogen from the subsurface is through chemical reaction processes: minerals such as olivine can react with water and transform to serpentine, generating hydrogen (known as white hydrogen or gold hydrogen, e.g., Barbier et al. 2020, Ellison et al. 2021, Klein et al. 2013, Lamadrid et al. 2017, McCollom et al. 2009, 2020, 2022, Osselin et al. 2022). This process can potentially produce 23 million tonnes of H_2 each year (Zgonnik, 2020)—an amount equal to almost a quarter of the current total hydrogen demand globally (IEA, 2021). To generate and produce H_2 from the subsurface economically, safely, and sustainably, a number of scientific questions arise that require advanced fundamental understanding. These include where and how deep to generate and extract H_2, how to maximize the generation rate, how to maximize the production rates with the best volume and purity, how to avoid hazards such as induced seismicity, and how to avoid loss of H_2 due to leakage and biogeochemical consumption during extraction. Among these questions, the key to the success of extracting geologic H_2 is to understand and control the flow of H_2 once it is generated.

Residual trapping refers to the portion of fluid that is rendered immobile (i.e. trapped) in the pore space as disconnected ganglia surrounded by brine in a storage aquifer. The trapping is controlled by the geometry of the pore and the physics of the fluid-fluid and solid-fluids interfaces (Krevor et al., 2015). Residual trapping can occur when capillary forces become the key controlling factor compared with other forces such as buoyancy, inertia and viscous forces that act on the wetting phases. It is important here to distinguish between the concepts of "occupancy" and "entrapment". After injecting a non-wetting fluid (such as H_2, CO_2) into a wetting-phase fluid-filled porous medium, the non-wetting fluid may occupy some portion of the pore space but may not be trapped. Taking CO_2 storage, for example, when CO_2 is injected into a porous medium, CO_2 can occupy the pore space by replacing the saline water, forming a large continuous plume (De Silva and Ranjith, 2012; Ershadnia et al., 2021; Suekane et al., 2008). After the CO_2 injection is stopped, saline water imbibes back into the pore space, breaking down the continuous CO_2 plume into disconnected parts around the walls of the solid materials. Only when the forces satisfy certain conditions can the CO_2 be trapped in the porous medium in the long term. In contrast, residual trapping is unique in the context of H_2 storage since H_2 storage involves cyclic storage and withdrawal of H_2. Both storage (drainage) and withdrawal (imbibition) will have a significant impact on residual trapping. Similar multiphase flow processes associated with extraction of H_2 also take place during geologic H_2 production, except that the rock types that are used for H_2 storage and generation are different. Since residual trapping plays an important role in all of these processes, in this study we will focus on the discussion of residual trapping of H_2 storage that considers cyclic injection and withdrawal, which also includes a simplified case for residual trapping of H_2 production.

Previous studies on residual trapping have summarized multiple pore-scale mechanisms that include bypassing (Dullien, 2012). "*Bypassing*" is a mechanism which gives rise to the entrapment of a non-wetting phase. It is also referred to as "pore doublet model" (Lundström et al., 2008; Zamula et al., 2019; Lake, 1989) in which the heterogeneity of two or more adjacent pores is considered (Lake, 1989). Here, if one of the adjacent pores becomes dead-end, we use the same terminology of "dead-end bypassing" to refer to the entrapment in a dead-end pore. It is widely reported that it is difficult to displace oil out of the dead-end pores (Guo et al., 2018; Iglauer et al., 2012; Fang et al., 2022). Dead-end bypassing trapping has also been directly visualized in microfluidic experiments. These experiments show that oil can be immobilized in dead-end pores while water flowed in the channel (Roman et al., 2017; Mehmani et al., 2019). However, the underlying mechanism of dead-end bypassing trapping has not been thoroughly investigated.

The aforementioned studies have advanced our understanding of residual trapping. However, due to the uniqueness of residual trapping in the context of H_2 storage and production, it is ideal to have the maximum occupancy of H_2 during storage (drainage) and minimum residual trapping during withdrawal (imbibition) stages. Specifically for pore-scale physics, it remains unclear under what geometric and physical conditions residual trapping can take place, and at what fraction of the pore space. Furthermore, these mechanisms are developed mostly based on oil/water systems, which start from oil-saturated situation since oil is generated in the pore space. In contrast to oil/water systems, H_2 is injected into the pore space rather than being generated in the pore space. This introduces the cyclic effect into the system. The cyclic drainage/imbibition effect has been reported to have a significant impact based on theory (Land 1968; Hassanizadeh and Gray, 1993; Pan et al., 2022), numerical modeling (Celia et al., 1993, 1995; Joekar-Niasar et al., 2013) and experiments (Porter et al., 2010; Herring et al., 2016, 2018, 2021). Yet, it is less commonly observed or predicted for gas storage as the non-wetting phase is injected rather than being generated in the pore space. For H_2 storage, residual trapping should be suppressed or minimized, in striking contrast with carbon sequestration. Due to the cyclic injection and withdrawal working gas, it remains unclear how drainage and imbibition along with the pore geometry impact the residual trapping. In other words, it is not straightforward how to extend the trapping mechanism at the pore scale when imbibition does not start from fully saturated conditions of the non-wetting phase in the context of hydrogen storage.

In this study, we aim to answer the following scientific question:

- *How do pore geometry, capillary force and injection/production flow rate affect residual trapping of H_2?*

To answer this scientific question, we use pore-scale simulations to provide quantitative predictions at various conditions. We extract a simplified, yet representative, pore geometry feature to study the trapping mechanism as shown in Fig. 1. In the case of a dead-end pore geometry (shown in the box with dashed outlines on the left of Fig. 1), we quantitatively investigate the percentage of non-wetting phase that can be trapped in the dead-end pore and study the impact of pore geometry and flow rate by both theoretical analysis and numerical simulations.

The paper is organized as follows. In Sections 2.1 and 2.2, the governing equations and the numerical approach are introduced. In Section

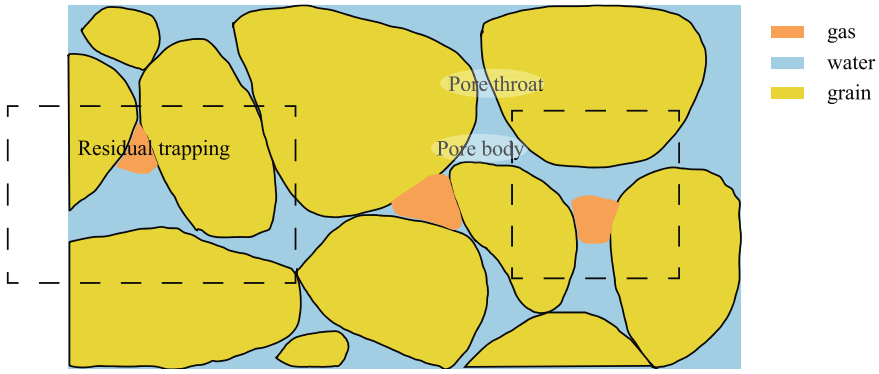

Fig. 1. Conceptual figure for residual trapping: schematic for multiphase flow in porous media.

3, we investigate both bypassing and trapping mechanisms through a combination of theoretical analysis and numerical simulations, and further analyze the impact of drainage on imbibition. Additionally, results on various pore geometries are presented. In Section 4, we compare different gases and discuss the "round corner effect". We then conclude the analysis by discussing the different implications of dead-end bypassing mechanism on both hydrogen storage and carbon sequestration.

2. Numerical approach

2.1. Governing equations

At the pore scale, the governing equations for two-phase immiscible flow include the conservation of mass and the conservation of momentum (i.e. the incompressible Navier-Stokes equations):

$$\nabla\cdot\boldsymbol{u}_i = 0 \tag{1}$$

$$\frac{\partial \boldsymbol{u}_i}{\partial t} + (\boldsymbol{u}_i\cdot\nabla)\boldsymbol{u}_i = -\frac{1}{\rho_i}\nabla p_i + \nu_i\nabla^2\boldsymbol{u}_i + \boldsymbol{g} \tag{2}$$

Here, subscript $i = 1, 2$ refers to fluid 1 (wetting phase) and fluid 2 (non-wetting phase), respectively; $\boldsymbol{u}_i$, ν_i, ρ_i and p_i are the velocity, kinematic viscosity, density and pressure in each phase. Note that we make the simplification that hydrogen has a constant density when the pressure change is only on the order of magnitude of a few *kPas*, despite the fact that strictly it is compressible fluid. Later in the simulation, it is found that the density will only change by less than 1 %.

On the interface Γ, continuity of velocity and force balance in both the normal and tangential directions hold, which yields,

$$\boldsymbol{u}_1 = \boldsymbol{u}_2 \tag{3}$$

$$(p_1 - p_2) + \boldsymbol{n}\cdot\left(\rho_1\nu_1\left(\nabla\boldsymbol{u}_1 + \nabla\boldsymbol{u}_1^T\right) - \rho_2\nu_2\left(\nabla\boldsymbol{u}_2 + \nabla\boldsymbol{u}_2^T\right)\right)\cdot\boldsymbol{n} = -\sigma\kappa \tag{4}$$

$$\boldsymbol{t}\cdot\left[\rho_1\nu_1\left(\nabla\boldsymbol{u}_1 + \nabla\boldsymbol{u}_1^T\right) - \rho_2\nu_2\left(\nabla\boldsymbol{u}_2 + \nabla\boldsymbol{u}_2^T\right)\right]\cdot\boldsymbol{n} = 0 \tag{5}$$

Here, n and t are the normal and tangential vectors to the interface $\boldsymbol{\Gamma}$; κ is the local curvature of the interface $\boldsymbol{\Gamma}$ and σ is the surface tension, which is a function of fluid types.

2.2. The volume of fluid approach

The volume of fluid (VOF) framework can be employed for the numerical solution of the multiphase system (Deshpande et al., 2012; Gopala et al., 2008; Shams et al., 2018). To track the moving interfaces between different phases, the phase fraction α is introduced to represent the phase fraction in each rectangular grid. As shown in Fig. 2a, when the grid is 100 % wetting phase, $\alpha = 1$. When the grid is 100 % non-wetting phase, $\alpha = 0$. If one or several interfaces (or a curved interface) cross a rectangular grid with 60 % wetting phase, $\alpha = 0.6$.

Using the phase fraction globally for a multiphase problem, the Navier-Stokes equations are written as:

$$\rho\left[\frac{\partial \boldsymbol{u}}{\partial t} + (\boldsymbol{u}\cdot\nabla)\boldsymbol{u}\right] = -\nabla p + \mu\nabla^2\boldsymbol{u} - \mathbf{g}\nabla\rho + \mathbf{f}_\sigma \tag{6}$$

Note that the fluid phases automatically shift between non-wetting ($\alpha = 0$) and wetting ($\alpha = 1$) when fluids are flowing over the domain. Thus, there are no distinct global variables of u between different phases. Here, f_σ is the capillary force due to the presence of two phases. The capillary force f_σ is a function of surface tension σ and local curvature κ of the interface. Surface tension σ is an intrinsic physical property depending upon the fluid types. ρ and μ are all functions of α.

The equation for conservation of mass reads

$$\nabla\cdot(\rho\boldsymbol{u}) = 0 \tag{7}$$

In addition, as the interfaces may be moving, α changes over time:

$$\frac{\partial\alpha}{\partial t} + \nabla\cdot(\alpha\boldsymbol{u}) + \nabla\cdot\left(\alpha(1-\alpha)c|\boldsymbol{u}|\frac{\nabla\alpha}{|\nabla\alpha|}\right) = 0 \tag{8}$$

Here, c is the compression factor which controls the magnitude of the last term. The last term is added to the equation for the purpose of compressing the interface between two phases to make it less diffusive. The interface can be tracked by the transition of the phase fraction field from 0 to 1. As shown in Fig. 2, we can infer the position of the interface by observing the distribution of phase fractions.

It is also worth mentioning that the continuum approximation is introduced to calculate the capillary pressure in the VOF framework. There is a sharp pressure change across the interface that might lead to divergence in numerical simulations. To address this, a continuum surface force model proposes a volumetric representation of surface tension f_σ in Eq. (6) as (Brackbill et al., 1992)

$$\mathbf{f}_\sigma = \nabla p_\sigma = \sigma\kappa\nabla\alpha \tag{9}$$

where p_σ is capillary pressure. Eqs. (6)–(9) are implemented into the InterFoam solver in OpenFOAM (Jasak et al., 2007).

2.3. Geometry and fluid properties

The behavior of multiphase flow in a single pore is fundamental for understanding multiphase flow in connected or disconnected pore network and real porous media. These individual pore geometric features are relevant to averaged properties of porous media. Dead-end pores may span across an entire porous medium (e.g., due to compaction), thus leading to a poor connection between different pores. Based on the definition (Dullien, 2012), connectivity decreases with the increase in the number of dead-end pores and height h. The aperture of a straight channel b is a good approximation of mean pore size and can further be related to permeability by the Carman-Kozeny equation

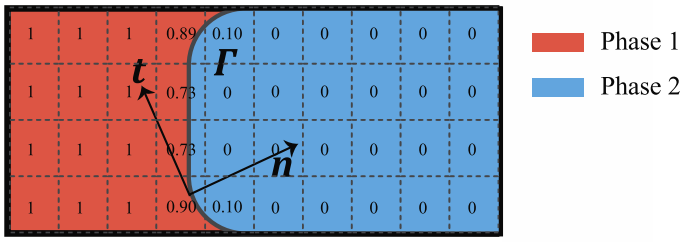

Fig. 2. Schematic for fluid domain, interface and phase fraction field distribution.

(Carman, 1997), for example. Thus, a quantitative understanding of how these pore geometry parameters can impact residual trapping provides useful insights at larger scales.

We begin the numerical experiments with single pores in rectangular shape to study the bypassing mechanism, as shown in Fig. 3. Even though the rectangular pore shape is a simplified scenario, it represents critical parameters that can be tuned including the aperture of a straight channel b, the height of dead-end pore h, the width of dead-end pore w, and the flow rate u. Further, these rectangular pores can be generalized for varied geometric features (such as deviation from perfect square or symmetric shapes).

Since the near wellbore region is our primary interest, the average flow velocity can be calculated from the average pumping rate. Here, we use an injection rate of $q_m = 1$Mt/yearfor hydrogen injection. The corresponding volumetric flow rate is $q_v = \frac{q_m}{\rho_{H_2}} = 3.17m^3/s$. If we approximate the well diameter d_w as $0.1m$, the Darcy velocityv_D is $v_D = q_v/(\pi d_w^2/4) = 404\ m/s$. The average pore velocity v_i would be approximately $v_i = \frac{v_D}{\phi} = 4040\ m/s$ in a porous medium with porosity ϕ of 0.1. This velocity would decay following a scaling relationship of $1/r^2$, where r is the distance from the wellbore. The pore velocity will decrease to $0.1m/s$ at $r = 200m$. In the simulation, we consider a range of velocities from 0.1 m/s to 5 m/s.

The dynamic properties of hydrogen and water at $T = 326K$, $p = 15MPa$ used as the input parameters for the simulation are obtained from NIST chemistry webbook, as summarized in Table 1.

3. Results

As residual trapping occurs in the drainage-imbibition cycle, in Section 3.1, we investigate the trapping percentage after imbibition from a stage that begins with full saturation with a non-wetting phase. In Section 3.2 we determine the percentage of non-wetting phase after drainage from fully wetting phase-saturated (water) state. Further, in Section 3.3 we study the residual trapping behavior in the full drainage-imbibition cycle by superimposing the process of drainage and imbibition. Finally, we investigate the results on converging and diverging dead-end pores.

3.1. Effects of pore geometry and injection on dead-end bypassing during imbibition

To understand the dead-end bypassing mechanism, we start with a theoretical analysis. In Geometry 1, an interface forms between the wetting phase and non-wetting phase during the displacement. When

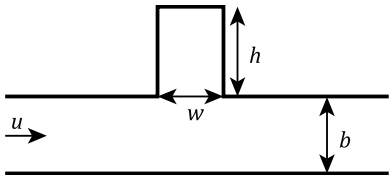

Fig. 3. Simplified geometry for a dead-end pore.

Table 1
Physical properties of fluid properties used in the simulation.

	H_2	H_2O
Density $\rho(kg/m^3)$	10.28	1000
Dynamic viscosity μ (cP)	0.00981	0.523
Kinematic viscosity ν (m^2/s)	9.5×10^{-7}	5.2×10^{-7}

the wetting phase is injected into a channel fully saturated by a non-wetting phase, the geometry and location of the advancing interface relevant to the solid boundaries of the dead-end pore are shown in Fig. 4a and b. The determining factor whether the non-wetting phase is trapped or not is the arrival time of the moving interface to point A and point B. If it arrives at point A first, all of the non-wetting phase existing in the dead-end pore initially will be ejected by the moving interface. In contrast, if it arrives at point B first, the interface will be split into two parts as shown in Fig. 4b. As a result, the non-wetting phase in the dead-end pore above the interface will remain trapped. In this geometry, the trapping percentage is governed by the ratio between arrival times to point A and point B. After the interface reaches point C, the rise of the moving interface is driven by the capillary force in the dead-end pore before the moving interface reaches either point A or point B. Hence, the scale of acceleration for the rise of the interface is given by

$$a_{\text{rising}} \sim \frac{\sigma}{h\rho(b+h)} \tag{10}$$

where σ is the surface tension. With the acceleration scale, time scale can be obtained as follows

$$t_A \sim \sqrt{\frac{h}{a_{\text{rising}}}} \sim \sqrt{\frac{h^2\rho(b+h)}{\sigma}} \tag{11}$$

The time scale of the interface's arrival at point B is

$$t_B \sim \frac{w}{u\frac{b}{b+h}} \tag{12}$$

Here, u is the injection flow rate. The scale of ratio between t_A and t_B is

$$\frac{t_A}{t_B} \sim \frac{h}{w}\frac{b}{b+h}\sqrt{\frac{\rho u^2(b+h)}{\sigma}} \tag{13}$$

where $\frac{h}{w}$ is the ratio of height to width. $\frac{\rho u^2(b+h)}{\sigma}$ is the ratio between inertial force and capillary force, which is a dimensionless number related to operating flow rate. If $b+h$ is chosen to be the representative length scale, $\frac{\rho u^2(b+h)}{\sigma}$ can be simplified to $CaRe$. The transition between trapping or not trapping occurs when $t_A \sim t_B$

$$\frac{h}{w}\frac{b}{b+h}\sqrt{CaRe} \sim 1 \tag{14}$$

Here, capillary number Ca and Reynolds number Re are defined as

$$Ca = \frac{\rho\nu u}{\sigma} \text{ and } Re = \frac{u(b+h)}{\nu} \tag{15}$$

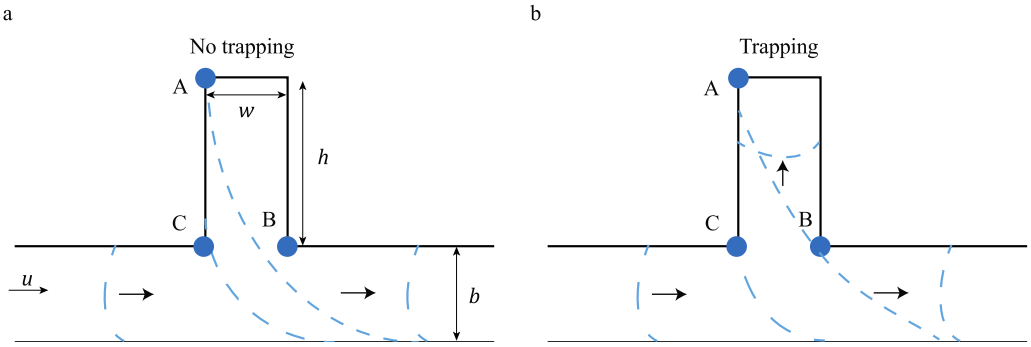

Fig. 4. (a). Schematic for scenario with no trapping (b). Schematic for scenario with trapping.

With the definition of Weber number $We = CaRe$, the transition condition in Eq. (15) can be further simplified to

$$\frac{h}{w}\frac{b}{b+h}\sqrt{We} \sim 1 \tag{16}$$

From this we can see that the trapping behavior is controlled by the geometric factor as well as the interplay between inertial force and capillary force represented by Weber number. Based on Eq. (15), we can see that for a given pore geometry, only when the injection flow rate (which represents the viscous and inertia forces) exceeds a threshold as a function of the capillary force can dead-end bypassing occur.

As the trapping percentage is dependent on the ratio of arrival times, the trapping percentage will be controlled by h/w and $We = CaRe$ as shown from the theoretical analysis. Two extreme cases related to these two factors are considered. The first case is when the dead-end pore height-to-width ratio, h/w, is infinitely large, which implies that it takes an infinitely long time for the wetting phase to cover the dead-end pore completely. This scenario contributes significantly to residual trapping. If $We = CaRe$ is extremely large at high flow rates, the wetting phase will penetrate the main channel without being able to enter the dead-end pore. To further verify the theoretical analysis and quantitatively determine the trapping percentage, high-fidelity simulations were conducted under different height-to-width ratios h/w and various flow rates to achieve different $We = CaRe$ numbers.

The simulation results confirm our theoretical analysis: whether the moving interface makes the first contact with point B or A determines whether the non-wetting phase is trapped or not. Specifically, as shown in Figs. 5a(II) and 6a(II), when the moving interface arrives at point A first, all of the non-wetting fluid is driven out of the dead-end pore, thus leading to no residual trapping (Figs. 5a(III) and 6a(III)). In contrast, when the interface arrives at point B first, residual trapping occurs (Figs. 5b(II-III) and 6b(II-III)). Notably, the only difference between two cases in Fig. 6 is the ratio of height to width ($\frac{h}{w}$), while the only difference between two cases in Fig. 6 is the injection velocity.

It is worth mentioning that the theoretical analysis presented here can be potentially extended to three-dimensional geometry in a similar fashion by considering the arrival times of the interface. However, the interface is represented by a surface instead of a curve and the arrival point in two-dimensional geometry will be represented by a line. The arrival time analysis should be based on the timescale when the interface intersects the solid boundary and when the surface of interface reaches the top of dead-end pore. Moreover, three-dimensional scenario will be equivalent to the superposition of infinite numbers of two-dimensional cross sections.

We can also track the trapping percentage η_1 under different conditions using the simulations. Trapping percentage η_1 in the dead-end pore is defined by

$$\eta_1 = \frac{V_{nw}}{wh} \tag{17}$$

Here, V_{nw} is the volume of non-wetting phase trapped in the dead-end pore, which is calculated from numerical simulations. As shown in Fig. 7a, η_1 increases with h/w in each curve and shows a trend approaching 1 when h/w becomes extremely large. Also, η_1 increases with respect to $CaRe$ under different h/w. Results from the simulations show good qualitative agreement with the theoretical analysis. Notably,

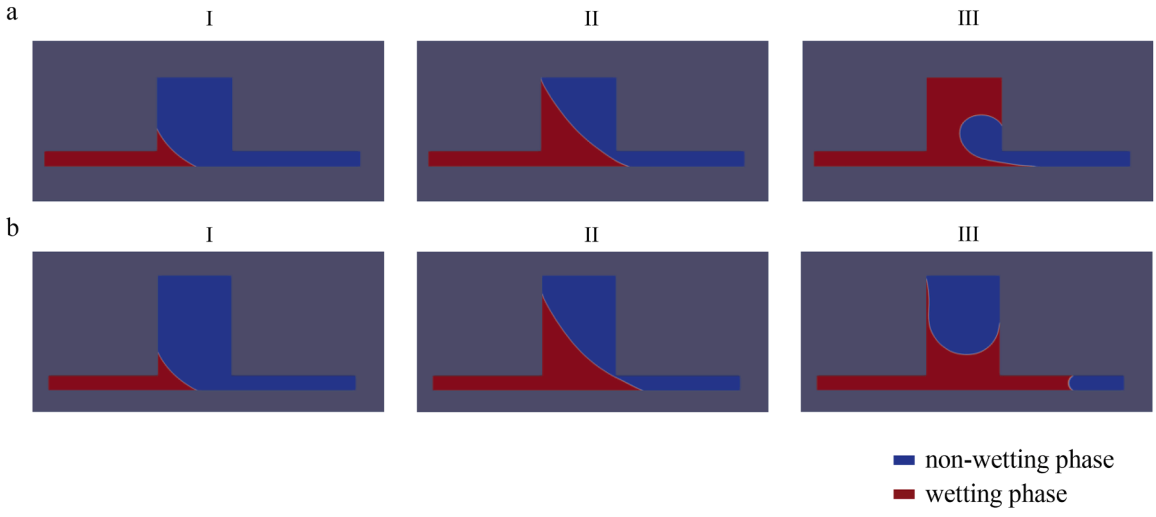

Fig. 5. Imbibition from a channel fully saturated with non-wetting phase (a) in a shallower pore with no non-wetting phase trapped in dead-end pore and (b) in a deeper pore with non-wetting phase trapped in dead-end pore.

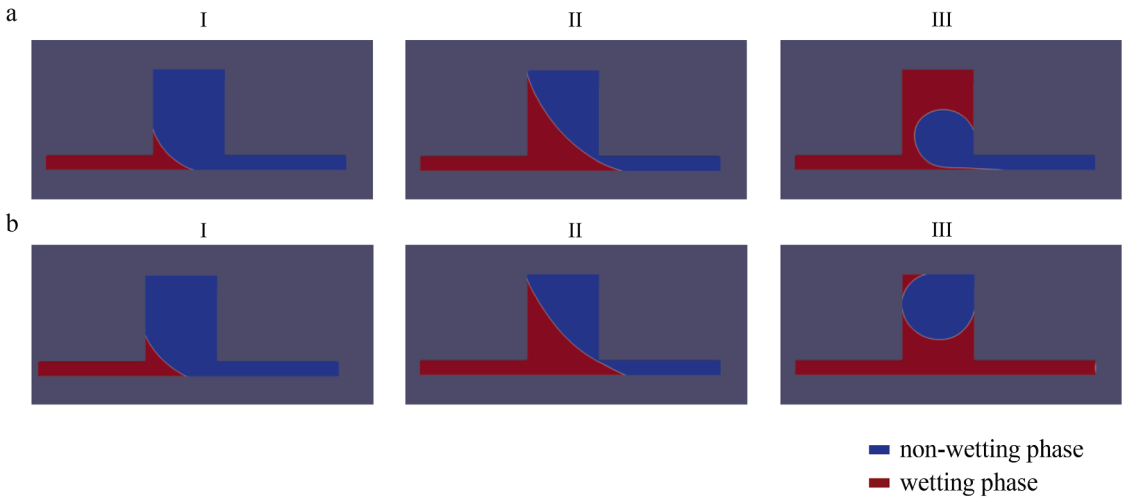

Fig. 6. Imbibition from a channel fully saturated with non-wetting phase (a) Injection velocity $u = 0.1m/s$ with no non-wetting phase trapped in dead-end pore and (b) Injection velocity $u = 0.5m/s$ with non-wetting phase trapped in dead-end pore.

though we find good qualitative agreement between our theoretical analysis and numerical simulations, it is difficult to achieve quantitative agreement. The time for the moving interface to reach point A or point B is only proposed for estimating their scales, but is not intended to capture the exact values. Moreover, the ratio of time scales cannot provide the exact trapping percentage though it reveals the important information on whether the entrapment will occur.

We can see that residual trapping behavior is controlled by h/w and $CaRe$ in such a geometry if imbibition is from a stage fully saturated with non-wetting phase. The relationship between $\eta_1$and h/wimplies that more dead-end pores and a higher aspect ratio can induce more residual trapping, which further suggests that both low connectivity and high connectivity can suppress residual trapping. The dependence on $CaRe$ implies that higher flow rate and larger pore size can lead to more residual trapping, which predicts that rapid imbibition in coarse porous media may cause significant residual trapping. Similarly, if we intend to mitigate residual trapping (e.g., withdraw more of the hydrogen that was stored from the subsurface), slow imbibition in tight porous media is preferred. However, these are idealized models and there are other constraints relating to the operating flow rate and the selection of storage formations for engineering purposes.

3.2. Dead-end bypassing of H_2 during a storage-withdrawal cycle

In the previous Section, we discussed the imbibition from a channel fully saturated with non-wetting phase. That is often unrealistic for underground hydrogen recovery from the storage. The consideration of drainage is non-trivial because the ultimate percentage occupying the porous media after drainage, which is also the initial saturation of imbibition, can impact the trapping behavior significantly. The extreme case of infinitely large h/w does not hold true because only a small portion of the dead-end pores is occupied by non-wetting fluid after drainage.

As Fig. 8a(i–iii) shows, there is some quantity of the wetting phase in the vicinity of a sharp corner that is difficult to displace due to the strong capillary force. To quantitatively investigate how much pore space is occupied after drainage, we define the occupying percentage η_2 as follows

$$\eta_2 = \frac{V_{nw}}{wh} \tag{18}$$

As shown in Fig. 8, there is a slight increase of η_2 when h/w is small because most of the dead-end pore space is taken up by non-wetting (except for any thin films that are present). If we assume the volume of thin film around the sharp corner is constant V_0,

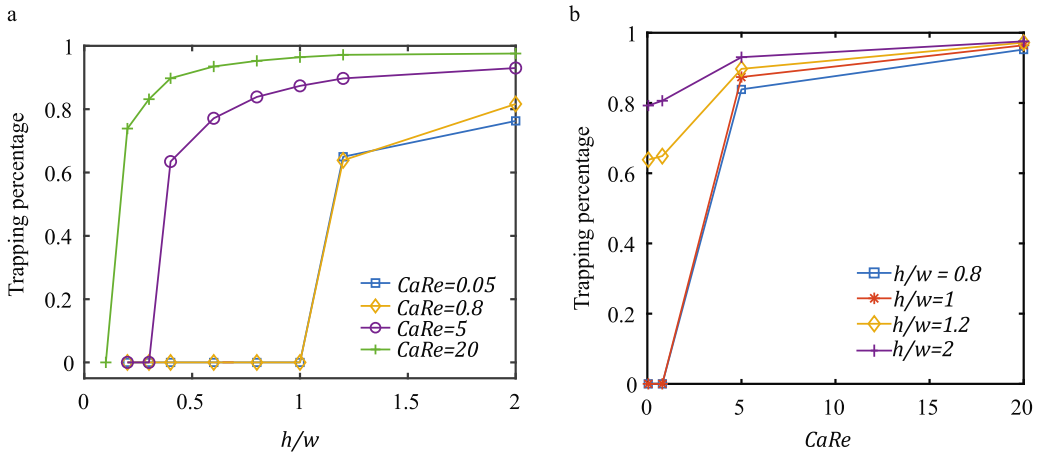

Fig. 7. (a) Relationship of trapping percentage η_1 at the end of imbibition with respect to h/w under different $CaRe$.(b) Relationship of trapping percentage η_1 at the end of imbibition with respect to $CaRe$ under different h/w.

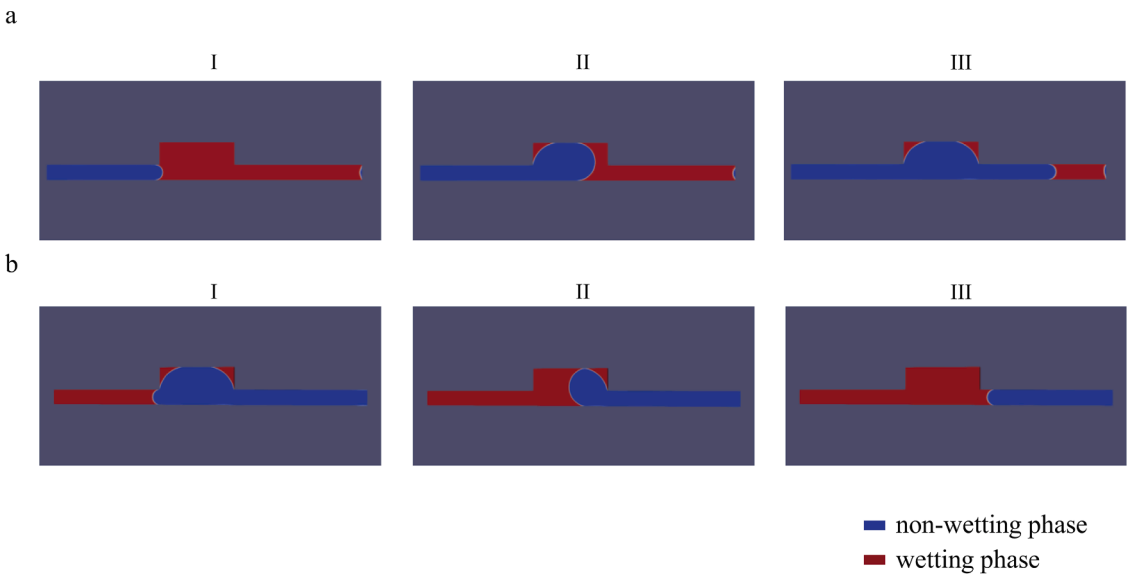

Fig. 8. (a). Drainage from a channel fully saturated with wetting phase (b). Imbibition from final stage of drainage (a(III)).

$$\eta_2 = 1 - \frac{V_0}{wh} \tag{19}$$

In the simulation, w is kept constant while h increases. Hence, η_2 increases when there is constantly thin wetting film.

As indicated in Fig. 9a, η_2 decreases with increasing h/w when h/w is greater than 0.4. The underlying reason is that in addition to the thin wetting film being close to the corner, a greater volume of wetting fluid near the end of the pore cannot be displaced compared with $h/w < 0.4$. If we compare the occupying percentage at different flow rates, we can see that lower flow rates will enhance the non-wetting fluid taking up the dead-end pore space asη_2 decreases with increasing$CaRe$.

These two relationships indicate that low operating flow rates during drainage are preferred if pore space is to be utilized to the maximum extent for subsurface storage purposes. In addition, drainage and imbibition show different impacts on the occupying percentage or trapping percentage with the increase of h/w. On one hand, a higher h/w provides larger pore space available for storage capacity for constant w. On the other hand, the lower occupying percentage of the pore volume stems from the higher h/w as observed in Fig. 9a. For an overall evaluation, the relationship between the percentage of non-wetting fluid in the dead-end pore and h/w is shown in Fig. 9b. Even though η_2 decays significantly with h/w, the occupying volume in the dead-end pore still rises due to the increase of dead-end pore volume.

3.3. Drainage-imbibition cycle

Based on the understanding of trapping and occupying mechanisms developed in the sections above, a more realistic injection-extraction cycle is presented in this section.

The gas injection period is characterized by a drainage process that begins with fully water-saturated conditions. The extraction period (Fig. 8b(I–III)) involves the injection of the wetting phase following the final stage of drainage with different geometry (h/w) and injection rates shown in (Fig. 8a(III)).

As shown in Fig. 9a, a slow injection rate corresponding to $CaRe = 0.002$ is used here to achieve maximum occupancy percentage. Fig. 10a shows a clear change in trend for different ranges of h/w as different processes dominate the trapping percentage. Hence, we divide the entire parameter space into two parts based on h/w, namely an imbibition-dominated regime and a drainage-dominated regime. Fig. 9a has shown that the saturation of a non-wetting phase at the end of drainage stage is approximately constant when $h/w < 0.4$ for slow drainage rates ($CaRe = 0.002$ and $CaRe = 0.05$). Given a constant initial saturation resulting from drainage, we can approximate the trapping percentage by simplifying the scenario to imbibition from a fully-saturated channel. As shown in Fig. 10a, the trapping percentage η_1 first increases with h/w when $h/w < 0.5$ corresponding to what has been shown in Fig. 7a. When

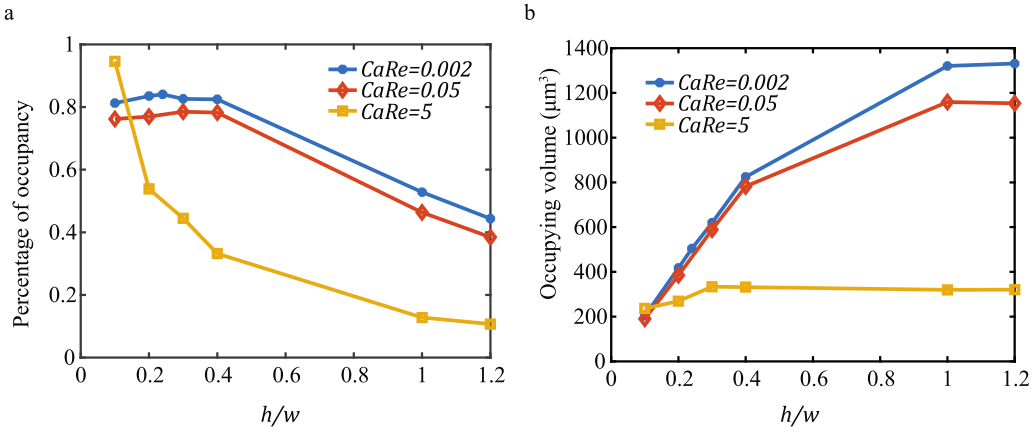

Fig. 9. (a). Relationship of occupying percentage of non-wetting phase η_2 at the end of drainage with respect to h/w under different $CaRe$ (b). Relationship between occupying volume of non-wetting phase at the end of drainage V_{nw}in the dead-end pore and h/w.

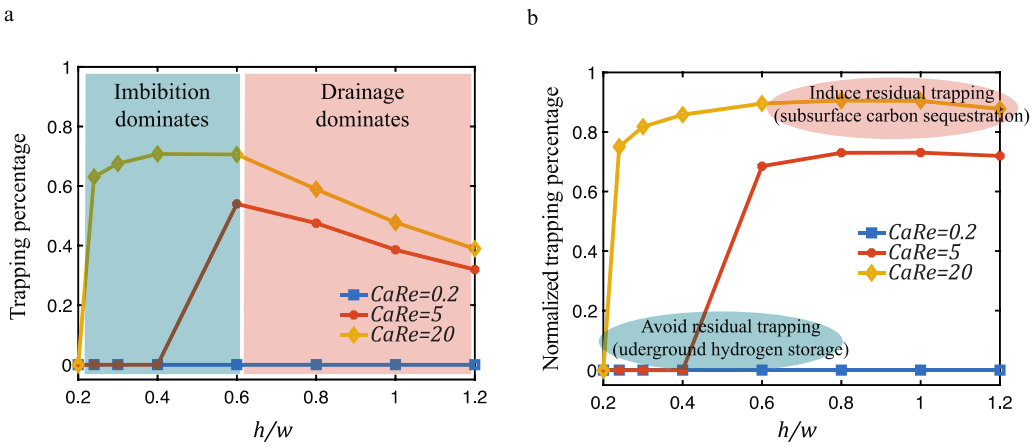

Fig. 10. (a). Relationship of trapping percentage η_1 with respect to h/w for different *CaRe* conditions (b). Relationship between the normalized trapping percentage $\overline{\eta_1}$ of the non-wetting phase for different h/w and *CaRe* cases.

$h/w > 0.5$, it is found that the trapping percentage begins to decrease because the ultimate trapping percentage is limited primarily by the lower initial saturation of the non-wetting phase.

To eliminate the impact of initial non-wetting phase saturation, we normalize the trapping percentage $\eta_1$with the final occupying percentage $\eta_2$as follows:

$$\overline{\eta_1} = \eta_1/\eta_2^f \tag{20}$$

where η_2^f is the final occupying percentage when drainage is completed.

After the trapping percentage is normalized, curves of $\overline{\eta_1}$ in Fig. 10b are found to be similar to those shown in Fig. 7a. It is apparent that two determining factors h/w and *CaRe* as analyzed in Section 3.1.1 continue to play a major role in determining the trapping percentage in the injection-extraction cycle.

3.4. Variations of pore-scale geometries

In previous discussions on dead-end bypassing mechanisms, the pore geometry of interest was rectangular dead-end pores as shown in Fig. 3a. In this section, we will demonstrate that the analysis and conclusions based on rectangular dead-end pores are applicable to more general scenarios that involve different pore geometries (the rule rather than exception in natural porous media). We conduct simulations on diverging and converging pores and explore their impacts on the trapping behavior. As Fig. 11 indicates, the width of the dead-end pore varies with the height while the total volume is kept constant in these simulations. To obtain a more detailed understanding, we investigate the trapping percentage for three scenarios: (1) both sides diverge/converge (2) the side closer to the inlet diverges/converges (3) the side further from inlet diverges/converges. These correspond to cases (1)-(3) in Fig. 11. The dash line in Fig. 11 indicates the rectangular dead-end pore as a comparison. Each dead-end pore has an entry line, as denoted in Fig. 11a(1). The imbibition begins with a stage where the saturation of H_2 is 100 %. Two representative dead-end pore height $h = 50\mu m$ (no trapping) and $h = 70\mu m$ (trapping) are simulated here. All the flow conditions are kept the same as in Fig. 5.

As Fig. 12 shows, when $h = 50\mu m$, trapping does not occur for a converging dead-end pore (like the rectangular pore) while trapping does occur for a diverging dead-end pore. To compare, no non-wetting phase is trapped for a rectangular dead-end pore (Fig. 5a). The underlying reason that divergence or convergence can have a large impact is because the distance that the interface needs to cover to reach point A becomes the length of left-hand wall and the capillary force is changed because of the diverging or converging width. As an approximation, the width of the entry line instead of the average width should be used for w in Eq. (13) and the length of left-hand wall should be used for h in Eq. (13).

As Fig. 13 shows, when $h = 70\mu m$, some amount of the non-wetting phase is trapped for both converging and diverging pores. Moreover, the trapping percentage after imbibition is affected by the pore geometries. The ultimate trapping percentage obtained from simulations are

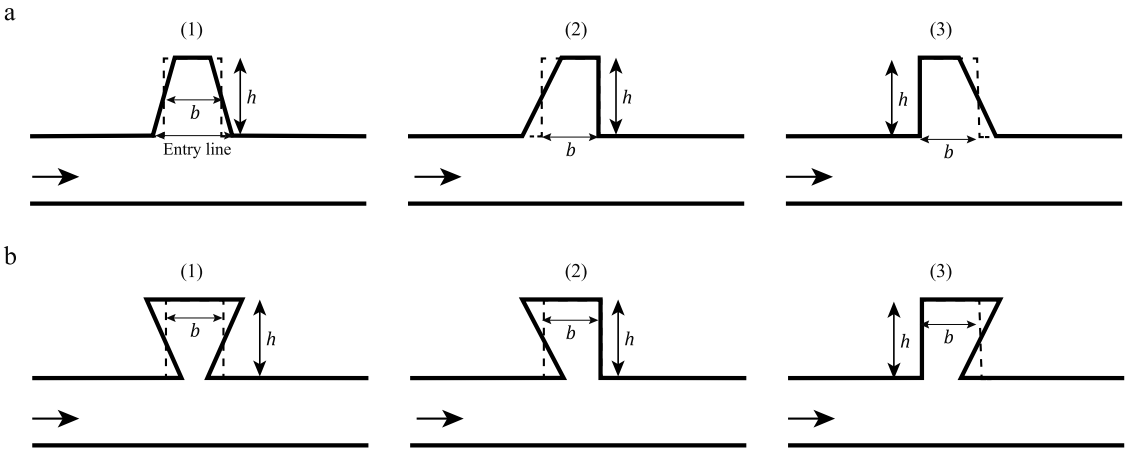

Fig. 11. Variations of pore geometries. (a). Converging dead-end pore where the width decreases with the height. (b) Diverging dead-end pore where the width increases with height.

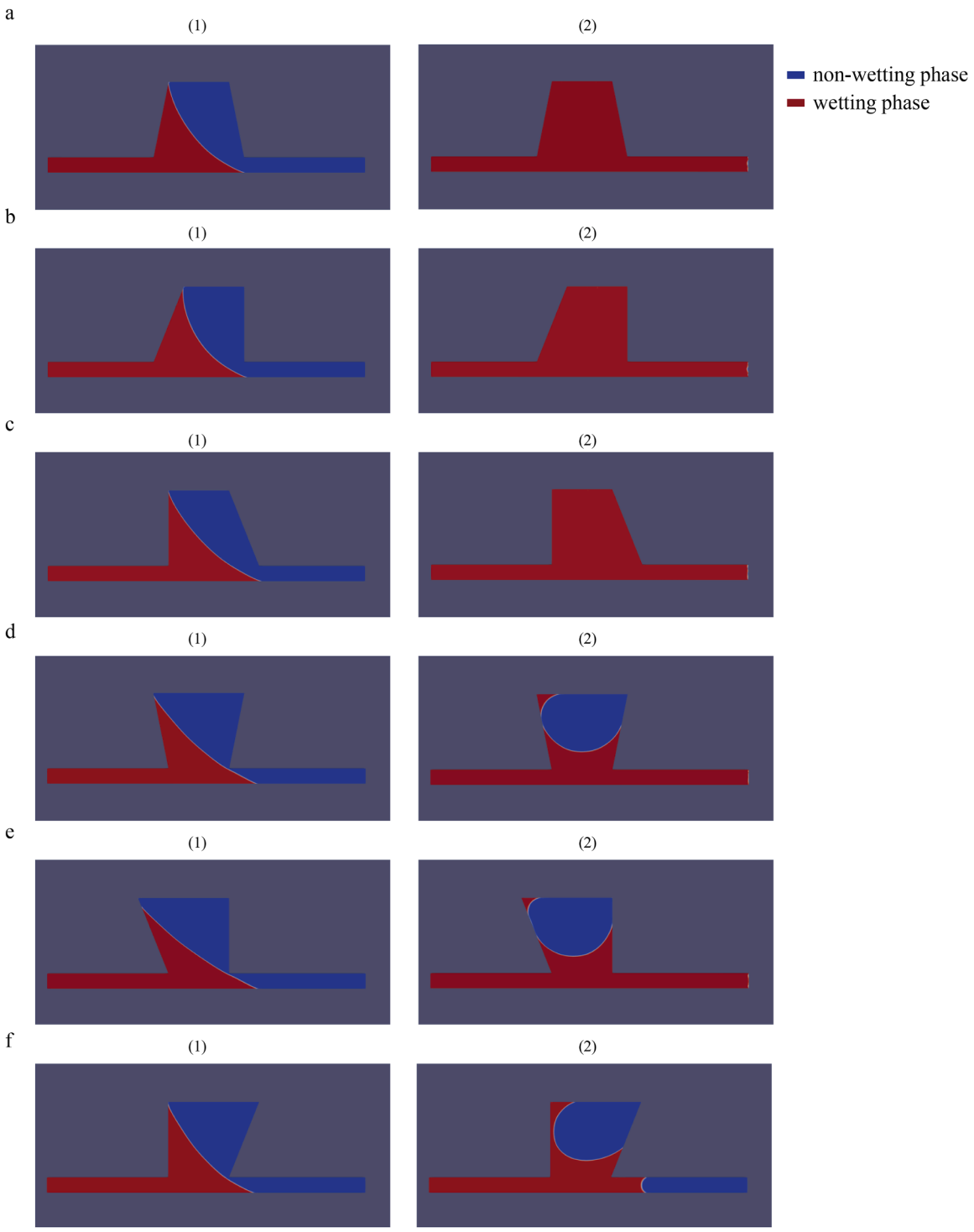

Fig. 12. Imbibition from a channel $h = 50\mu m$ fully saturated with non-wetting phase: (a)–(c) Three converging pore geometries corresponding to those shown in Fig. 11a. (d)–(f) Three diverging pore geometries corresponding to those shown in Fig. 11b. (1) The configuration when the moving interface reaches point A or point B. (2) The ultimate configuration after imbibition.

compared for the different pore geometries. As shown in Fig. 14, the relationship of trapping percentage with respect to pore geometries can be summarized as: diverging pores> rectangular pores> converging pores. This relationship agrees with our approximation that the width of entry line should be used for w. Moreover, if the diverging side is closer to the inlet, the trapping percentage will be higher as we can see from scenario (2) that has the largest trapping percentage under the same condition. This relationship verifies our approximation that the length of left-hand wall should be used for h in Eq. (13). Despite the large difference in geometry between converging, diverging and rectangular shaped pores that can be explained by the differences in the values of h/w, we do not see notable differences in trapping volume caused by the pore structure inside a converging or a diverging wall. This is demonstrated by similar volumes predicted for scenarios (1)–(3) for both converging and diverging pores in Fig. 14. We conclude that despite the differences in the detailed pore structure (such as scenarios (1)–(3)), h/w

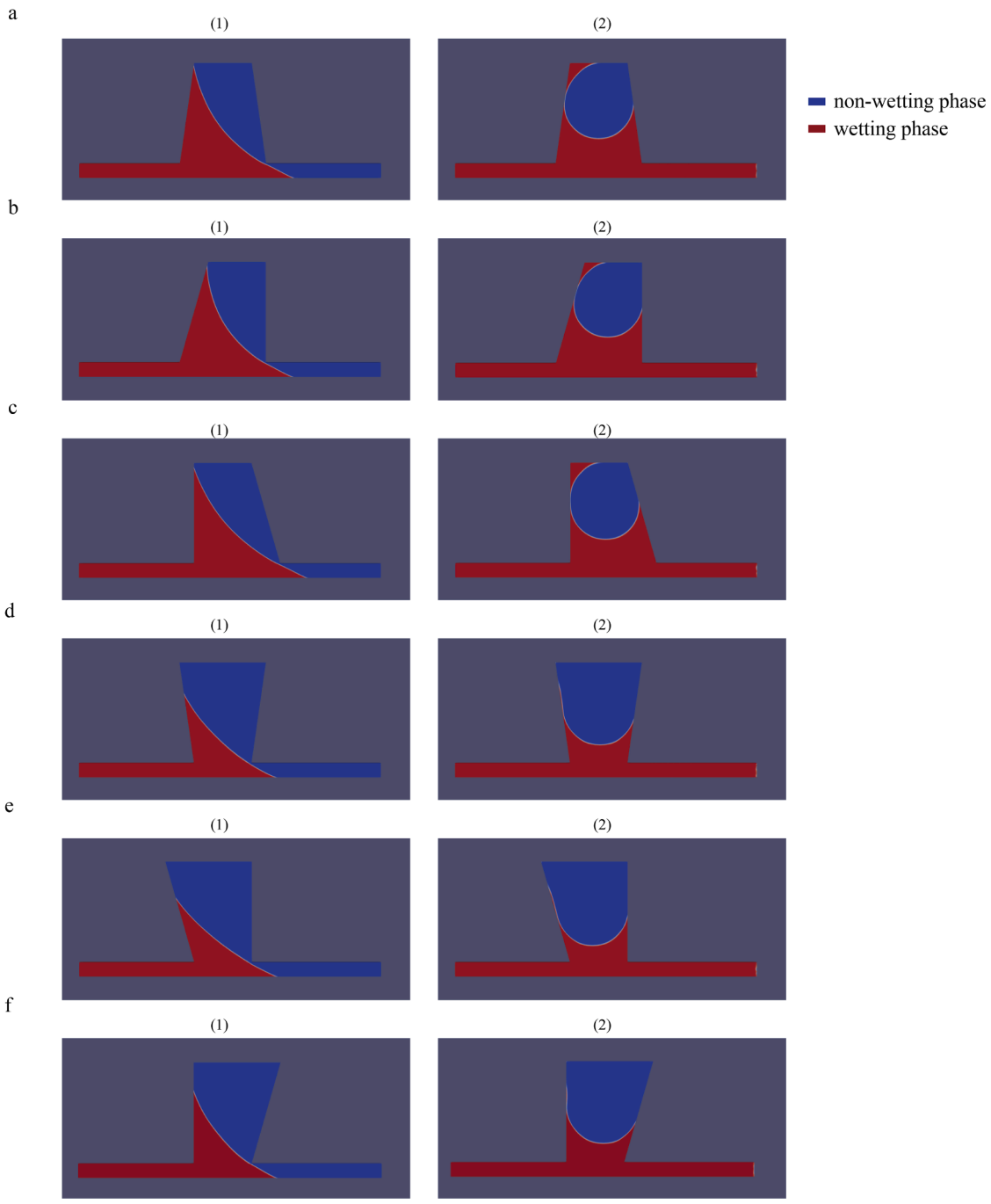

Fig. 13. Imbibition from a channel $h = 70\mu m$ fully saturated with non-wetting phase: (a)–(c) Three converging pore geometries corresponding to those shown in Fig. 14a. (d)–(f) Three diverging pore geometries corresponding to those shown in Fig. 14b. (1) The configuration when the moving interface reaches point A or point B. (2) The ultimate configuration after imbibition.

is the key controlling factor of pore geometry determining the occurrence and percentage of residual trapping.

From the discussion and figures above, we can see that the underlying mechanism of dead-end bypassing is governed by the time that the moving interface reaches point A or point B as illustrated in Fig. 4. Due to the diverging pore geometry, the time scale for the interface to reach Point B is shortened, thus potentially contributing to more dead-end bypassing trapping. This explains why trapping occurs for diverging pores at $h = 50\mu m$.

For converging dead-end pore, the opposite effect occurs. The time for the interface to arrive at Point B increases. To the extent that our hypothesis illustrated in Fig. 4 holds for other pore geometries, the analysis can be extended to more general cases.

4. Discussion

4.1. Comparison between different gases

We focus primarily on the H_2-water system in the previous analysis, although the analysis can be generalized to the CO_2/water system as well. Table 2 shows the physical properties of H_2, CO_2 and N_2.

If two-phase immiscible flow is assumed, the pore-scale flow physics will still follow our analysis. The contact angles of these two types of gases are close and thus the moving interface geometry will be similar.

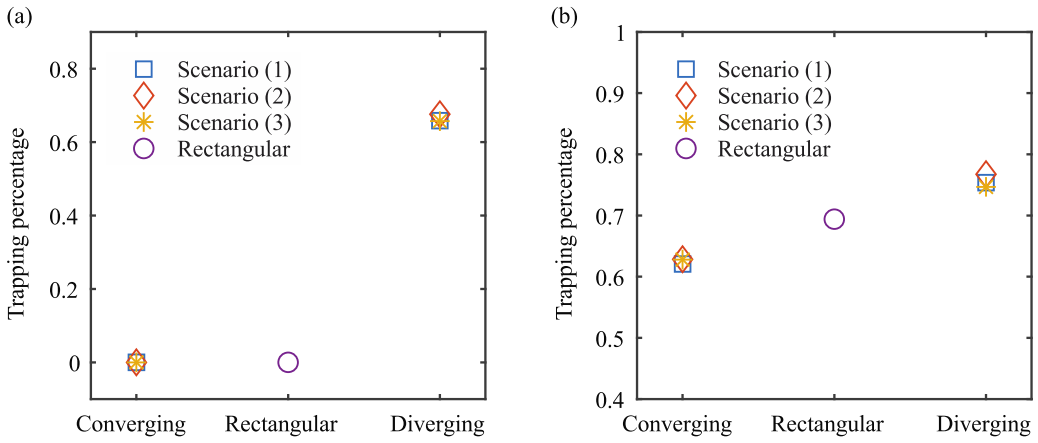

Fig. 14. (a). Trapping percentage of pore geometries when $h = 50\mu m$ (b). Trapping percentage of pore geometries when $h = 70\mu m$. Scenario (1)–(3) correspond to those shown in Fig. 11 (1)–(3).

However, some parameters will be different due to the alteration of the physical properties. The ratio of impacting factor *CaRe* under the same velocity will be

$$\frac{Ca\ Re(H_2)}{Ca\ Re(CO_2)} = 0.51,\quad \frac{Ca\ Re(N_2)}{Ca\ Re(CO_2)} = 0.542,\quad \frac{Ca\ Re(H_2)}{Ca\ Re(N_2)} = 0.93 \tag{25}$$

We can see that *CaRe* of H_2 and N_2 is approximately the half of that of CO_2, but of a similar order of magnitude. This means that CO_2 is more likely to be trapped under the same pore geometries and working conditions. In the literature, some experiments suggest using N_2 as a substitute for CO_2 to study the multiphase behavior because N_2 is easier to use (Thaysen et al., 2023; Niu et al., 2015). Based on the theoretical analysis, these two gases will have very similar flow and trapping behavior, but N_2 as a substitute can underestimate the trapping percentage due to dead-end bypassing mechanism. It is also worth mentioning that H_2 and CO_2 will have additional dissimilarities in terms of chemical properties and upscaling pore-scale flow physics to the Darcy scale.

4.2. Round corner effect

One assumption we make in the theoretical analysis is that the interface will break up into two parts once it reaches point B in Fig. 4. Our simulation results presented above verify that the interface is pinched at the corner, leading to interface breakup.

To further verify our assumption under the conditions of a round corner, we use a polyline consisting of obtuse angles to replace the sharp corner, as shown in Fig. 15. The reason we choose polylines is because there is no ideal round corner in nature and the surface is rough at the pore scale. The height of the channel is taken as $50\mu m$ and $70\mu m$ to be consistent with the results in Section 3.4.

As shown in Fig. 16, there will be no trapping for the scenarios where $h = 50\mu m$. The interface will still arrive at the top of the dead-end pore first. The rounded corners will not affect the trapping percentage results of the trapping percentage when there is no trapping behavior predicted for the pore structure with sharp corner. Furthermore, when $h = 70\mu m$, the moving interface will still break up into two parts when it arrives at point B as we can see from Fig. 17. For both pore geometries, there will be trapping of non-wetting phase in the dead-end pore after the imbibition. This test validates that the dead-end bypassing mechanism still applies when the corners are not sharp.

Table 2
Physical properties of H_2, CO_2 and N_2 at $T = 326K$, $p = 15MPa$.(Hosseini et al., 2022; Linstrom and Mallard, 2001; Hashemi et al., 2022; Li and Fan, 2015; Niu et al., 2015; Hashemi et al., 2021).

	H_2	CO_2	N_2
Density ρ (kg/m^3)	10.28	672	148
Dynamic viscosity μ (cP)	0.00981	0.053	0.022
Kinematic viscosity ν (m^2/s)	9.5×10^{-7}	7.9×10^{-8}	1.49×10^{-7}
Surface tension with water (mN/m)	68	35	73
Contact angle with water and sandstone	36	30	45

4.3. Applications of trapping mechanisms

In the previous two sections, two mechanisms of residual trapping were investigated by theoretical analysis and numerical simulation. In this section, applications of these mechanisms to engineering problems are discussed.

The dead-end bypassing mechanisms we have elucidated have important implications for different engineering applications. Our findings, summarized in Fig. 18, suggest that a low drainage flow rate is recommended for porous media with low h/w to maximize pore space utilization, while a low drainage flow rate is suggested for porous media with high h/w to maximize storage capacity. For underground hydrogen storage, a low imbibition flow rate is necessary in geological formations with low h/w to suppress residual trapping and achieve high recovery rates. For geologic hydrogen production, there is a trade-off between reactive surface and recovery rate. If the reaction is rapid leading to high saturation of hydrogen in the pore, a low imbibition flow rate on a porous medium with high h/w is preferred. If the production is significantly limited by the reaction rate, a low imbibition flow rate on a porous medium with low h/w will have greater amount of hydrogen recovered. In contrast, subsurface carbon sequestration requires a high imbibition flow rate and high h/w to induce residual trapping and immobilization of the injected carbon dioxide.

The overall trapping percentage will be dependent on the properties of the porous media. If there are a large number of dead-end pores present, the dead-end bypassing mechanism will dominate residual trapping. Insights on the selection of the optimal geological formation for a particular engineering application can be gained based on the understanding of the pore structure and the impact of the selected mechanism on residual trapping. This in turn could provide guidance on the selection of geological formations for different purposes. Both mechanisms are part of residual trapping, which is a more secure trapping mechanism compared with structural trapping (Krevor et al., 2015). The dead-end pores primarily play a role over shorter time scales compared with mineral trapping. We conclude that a thorough investigation on the pore-scale features of the geological formation and the distribution of dead-end pores and pore throats can be very helpful by providing prior knowledge to be used engineering analyses.

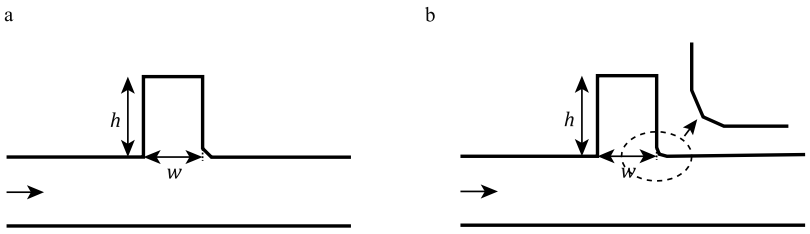

Fig. 15. Pore geometry with the sharp corners rounded by (a). one line (b) two-segment polyline.

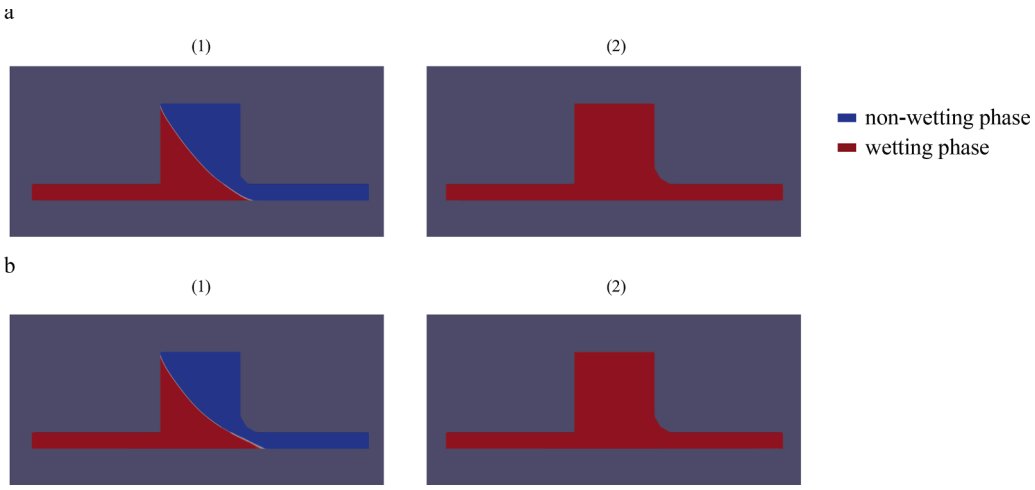

Fig. 16. Imbibition from a channel $h = 50\mu m$ fully saturated with non-wetting phase: (a)-(b) corresponding to the pore geometries shown in Fig. 15a and Fig. 15b, respectively. (1) The configuration when the moving interface reaches point A or point B. (2) The ultimate configuration after imbibition.

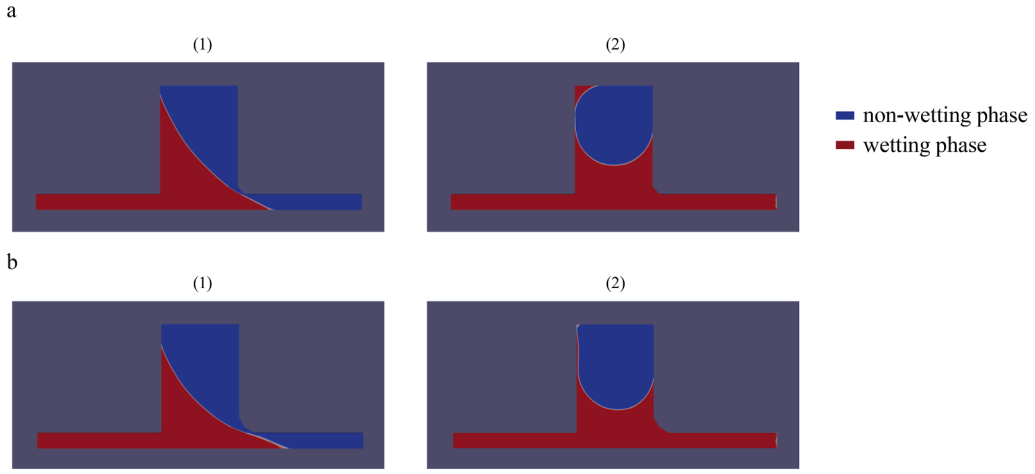

Fig. 17. Imbibition from a channel $h = 70\mu m$ fully saturated with non-wetting phase: (a)-(b) corresponding to the pore geometries shown in Fig. 15a and Fig. 15b, respectively. (1) The configuration when the moving interface reaches point A or point B. (2) The ultimate configuration after imbibition.

5. Conclusions

In this study, we have made a first attempt to conduct pore-scale modeling to investigate the effects of pore geometry and injection rate on the occurrence and percentage of residual trapping of hydrogen via dead end. We began our theoretical and numerical analyses with a single rectangular dead-end pore to understand the key controls in dead-end bypassing. We further investigated two factors on dead-end bypassing: (a) a continuous cycle of injection-extraction of H_2, and (b) varied pore geometry.

For a dead-end bypassing mechanism, we proposed a scaling law to determine the entrapment based on the arrival time scales of the moving interface and verify the theoretical analysis with numerical simulations. We demonstrated that:

- Ø The trapping percentage due to dead-end bypassing is governed by two dimensionless numbers h/w and $We = CaRe$, which indicates that higher aspect ratio of dead-end pore and higher injection flow rate will induce residual trapping if simplification that imbibition starts from fully saturated with non-wetting phase is made.
- Ø In an injection-extraction cycle, we found trapping percentage increases with h/w first in the imbibition-dominated regime and then decreases after h/w reaches 0.5 in the drainage-dominated regime

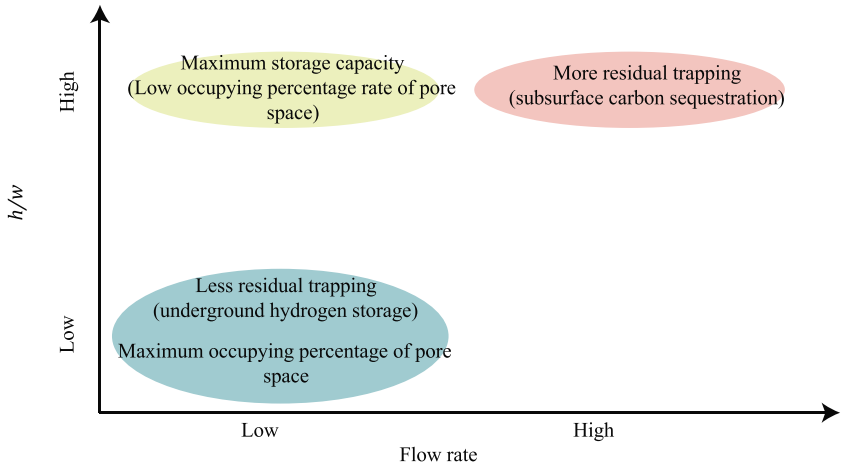

Fig. 18. Implications of dead-end bypassing mechanism on the selection of flow rate and porous media.

since the ultimate trapping percentage reflects the overall results of drainage and imbibition.

Ø With the same volume of a dead-end pore, a converging-shaped pore can result in less trapping volume and a diverging-shaped pore can result in more trapping volume, regardless of the differences in the detailed structure inside a pore.

These findings are not only complementary to fundamental multi-phase flow physics in porous media but also can be used to help optimize the storage, production, and sequestration processes. Based on a dead-end bypassing mechanism, underground hydrogen storage should make use of a porous media with low h/w under low flow rate while subsurface carbon sequestration should be operated in a porous media with high h/w and high flow rate. Since reaction is involved in geologic hydrogen production, there will be a trade-off between reactive surface and recovery rate. Depending on the reaction rate, geologic hydrogen production might have a good overall performance under low recovery rate on low or high h/w. The 2D modeling presented here at the scale of the hydrogen-water-solid interface provides quantitative understanding of dead-end bypassing mechanisms. However, two important questions remain considering potential 3D effects and the compressibility of hydrogen: (1) does the 3rd dimension introduce additional residual trapping mechanism that cannot be described in 2D? (2) How would the compressibility of hydrogen and miscibility of the interface affect all of these results? To answer these questions, we will extend the solver to miscible two-phase flow and conduct 3D analysis in the future. Moreover, there are other residual trapping mechanisms like snap-off. Other important questions to study include how to quantitatively describe snap-off at the pore scale. While there is practical variability in terms of flow rates and porous media types are highly variable in natural systems, our study will be useful for developing engineering controls of H_2 storage and production.

CRediT authorship contribution statement

Siqin Yu: Conceptualization, Methodology, Software, Validation, Formal analysis, Investigation, Data curation, Writing – original draft, Writing – review & editing, Visualization. **Mengsu Hu:** Conceptualization, Methodology, Formal analysis, Investigation, Resources, Writing – original draft, Writing – review & editing, Supervision, Project administration, Funding acquisition. **Carl I. Steefel:** Conceptualization, Methodology, Formal analysis, Investigation, Resources, Writing – original draft, Writing – review & editing, Supervision. **Ilenia Battiato:** Investigation, Resources, Writing – review & editing.

Declaration of competing interest

The authors declare that they have no known competing financial interests or personal relationships that could have appeared to influence the work reported in this paper.

Data availability

Data will be made available on request.

Acknowledgments

This work was supported by the Director, Office of Science, Basic Energy Sciences, Chemical Sciences, Geosciences, and Biosciences Division, of the U.S. Department of Energy under Contract No. DE-AC02-05CH11231 to Lawrence Berkeley National Laboratory. We would also like to thank two anonymous reviewers for providing the valuable suggestions.

References

Barbier, S., Huang, F., Andreani, M., Tao, R., Hao, J., Eleish, A., Daniel, I., 2020. A review of H_2, CH_4, and hydrocarbon formation in experimental serpentinization using network analysis. Front. Earth. Sci. 8, 209 (Lausanne).

Birol, F. (2019). The future of hydrogen: seizing today's opportunities. IEA Report prepared for the G20. https://www.iea.org/reports/the-future-of-hydrogen.

Boon, M., Hajibeygi, H., 2022. Experimental characterization of [... formula...]/water multiphase flow in heterogeneous sandstone rock at the core scale relevant for underground hydrogen storage (UHS). Sci. Rep. 12, 14604.

Brackbill, J.U., Kothe, D.B., Zemach, C., 1992. A continuum method for modeling surface tension. J. Comput. Phys. 100 (2), 335–354.

Carman, P.C., 1997. Fluid flow through granular beds. Chem. Eng. Res. Des. 75, S32–S48.

Celia, M.A., Rajaram, H., Ferrand, L.A., 1993. A multi-scale computational model for multiphase flow in porous media. Adv. Water Resour. 16 (1), 81–92.

Celia, M.A., Reeves, P.C., Ferrand, L.A., 1995. Recent advances in pore scale models for multiphase flow in porous media. Rev. Geophys. 33 (S2), 1049–1057.

De Silva, P.N.K., Ranjith, P.G., 2012. A study of methodologies for CO_2 storage capacity estimation of saline aquifers. Fuel 93, 13–27.

Deshpande, S.S., Anumolu, L., Trujillo, M.F., 2012. Evaluating the performance of the two-phase flow solver interFoam. Comput. Sci. Discov. 5 (1), 014016.

Dopffel, N., Mayers, K., Kedir, A., et al., 2023. Microbial hydrogen consumption leads to a significant pH increase under high-saline-conditions: implications for hydrogen storage in salt caverns. Sci. Rep. 13, 10564.

Dullien, F.A., 2012. Porous Media: Fluid Transport and Pore Structure. Academic press.

Eddaoui, N., Panfilov, M., Ganzer, L., Hagemann, B., 2021. Impact of pore clogging by bacteria on underground hydrogen storage. Transp. Porous Media 139, 89–108.

Ellison, E.T., Templeton, A.S., Zeigler, S.D., Mayhew, L.E., Kelemen, P.B., Matter, J.M., Oman Drilling Project Science Party, 2021. Low-temperature hydrogen formation during aqueous alteration of serpentinized peridotite in the Samail ophiolite. J. Geophys. Res. Solid Earth 126 (6), e2021JB021981.

Ershadnia, R., Hajirezaie, S., Amooie, A., Wallace, C.D., Gershenzon, N.I., Hosseini, S.A., Soltanian, M.R., 2021. CO_2 geological sequestration in multiscale heterogeneous

aquifers: effects of heterogeneity, connectivity, impurity, and hysteresis. Adv. Water Resour. 151, 103895.
Fang, Y., Yang, E., Guo, S., Cui, C., Zhou, C., 2022. Study on micro remaining oil distribution of polymer flooding in Class-II B oil layer of Daqing Oilfield. Energy 254, 124479.
Gopala, V.R., Van Wachem, B.G., 2008. Volume of fluid methods for immiscible-fluid and free-surface flows. Chem. Eng. J. 141 (1–3), 204–221.
Guo, C., Wang, X., Wang, H., He, S., Liu, H., Zhu, P., 2018. Effect of pore structure on displacement efficiency and oil-cluster morphology by using micro computed tomography (μCT) technique. Fuel 230, 430–439.
Hand, E., 2023. Hidden hydrogen. Science 379 (6633), 630–636 (New York, NY).
Hashemi, L., Blunt, M., Hajibeygi, H., 2021a. Pore-scale modelling and sensitivity analyses of hydrogen-brine multiphase flow in geological porous media. Sci. Rep. 11 (1), 8348.
Hashemi, L., Boon, M., Glerum, W., Farajzadeh, R., Hajibeygi, H., 2022. A comparative study for H_2–CH_4 mixture wettability in sandstone porous rocks relevant to underground hydrogen storage. Adv. Water Resour. 163, 104165.
Hashemi, L., Glerum, W., Farajzadeh, R., Hajibeygi, H., 2021b. Contact angle measurement for hydrogen/brine/sandstone system using captive-bubble method relevant for underground hydrogen storage. Adv. Water Resour. 154, 103964.
Hassanizadeh, S.M., Gray, W.G., 1993. Thermodynamic basis of capillary pressure in porous media. Water Resour. Res. 29 (10), 3389–3405.
Hassannayebi, N., Azizmohammadi, S., De Lucia, M., Ott, H., 2019. Underground hydrogen storage: application of geochemical modelling in a case study in the Molasse Basin, Upper Austria. Environ. Earth Sci. 78, 1–14. Chicago.
Hassanpouryouzband, A., Joonaki, E., Edlmann, K., Haszeldine, R.S., 2021. Offshore geological storage of hydrogen: is this our best option to achieve net-zero? ACS Energy Lett. 6, 2181–2186.
Heinemann, N., Alcalde, J., Miocic, J.M., Hangx, S.J., Kallmeyer, J., Ostertag-Henning, C., Rudloff, A., 2021. Enabling large-scale hydrogen storage in porous media–the scientific challenges. Energy Environ. Sci. 14 (2), 853–864.
Herring, A.L., Andersson, L., Wildenschild, D., 2016. Enhancing residual trapping of supercritical CO_2 via cyclic injections. Geophys. Res. Lett. 43 (18), 9677–9685.
Herring, A.L., Gilby, F.J., Li, Z., McClure, J.E., Turner, M., Veldkamp, J.P., Sheppard, A. P., 2018. Observations of nonwetting phase snap-off during drainage. Adv. Water Resour. 121, 32–43.
Herring, A.L., Sun, C., Armstrong, R.T., Li, Z., McClure, J.E., Saadatfar, M., 2021. Evolution of bentheimer sandstone wettability during cyclic scCO_2-brine injections. Water Resour. Res. 57 (11), e2021WR030891.
Hosseini, M., Fahimpour, J., Ali, M., Keshavarz, A., Iglauer, S., 2022. H_2− brine interfacial tension as a function of salinity, temperature, and pressure; implications for hydrogen geo-storage. J. Pet. Sci. Eng. 213, 110441.
Hu, M., Steefel, C.I., Rutqvist, J., 2021. Microscale mechanical-chemical modeling of granular salt: insights for creep. J. Geophys. Res. Solid Earth 126 (12) e2021JB023112.
IEA, 2021. Global Hydrogen Review 2021. https://www.iea.org/reports/global-hydrogen-review-2021. License: CC BY 4.0.
Iglauer, S., Fernø, M.A., Shearing, P., Blunt, M.J., 2012. Comparison of residual oil cluster size distribution, morphology and saturation in oil-wet and water-wet sandstone. J. Colloid Interface Sci. 375 (1), 187–192.
Jangda, Z., Menke, H., Busch, A., Geiger, S., Bultreys, T., Lewis, H., Singh, K., 2023. Pore-scale visualization of hydrogen storage in a sandstone at subsurface pressure and temperature conditions: trapping, dissolution and wettability. J. Colloid Interface Sci. 629, 316–325.
Jasak, H., Jemcov, A., Tukovic, Z., 2007. OpenFOAM: A C++ library for complex physics simulations. In: Proceedings of the International Workshop on Coupled Methods in Numerical Dynamics, 1000, pp. 1–20. Vol.
Joekar-Niasar, V., Doster, F., Armstrong, R.T., Wildenschild, D., Celia, M.A., 2013. Trapping and hysteresis in two-phase flow in porous media: a pore-network study. Water Resour. Res. 49 (7), 4244–4256.
Klein, F., Bach, W., McCollom, T.M., 2013. Compositional controls on hydrogen generation during serpentinization of ultramafic rocks. Lithos 178, 55–69.
Krevor, S., Blunt, M.J., Benson, S.M., Pentland, C.H., Reynolds, C., Al-Menhali, A., Niu, B., 2015. Capillary trapping for geologic carbon dioxide storage–From pore scale physics to field scale implications. Int. J. Greenh. Gas Control 40, 221–237.
Lake, L.W. (1989). Enhanced oil recovery.
Lamadrid, H.M., Rimstidt, J.D., Schwarzenbach, E.M., Klein, F., Ulrich, S., Dolocan, A., Bodnar, R.J., 2017. Effect of water activity on rates of serpentinization of olivine. Nat. Commun. 8 (1), 16107.
Land, C.S., 1968. Calculation of imbibition relative permeability for two-and three-phase flow from rock properties. Soc. Pet. Eng. J. 8 (02), 149–156.
Li, X., Fan, X., 2015. Effect of CO_2 phase on contact angle in oil-wet and water-wet pores. Int. J. Greenh. Gas Control 36, 106–113.
Linstrom, P.J., Mallard, W.G., 2001. The NIST chemistry WebBook: a chemical data resource on the internet. J. Chem. Eng. Data 46 (5), 1059–1063.
Liu, N., Kovscek, A.R., Fernø, M.A., Dopffel, N., 2023. Pore-scale study of microbial hydrogen consumption and wettability alteration during underground hydrogen storage. Front. Energy Res. 11, 1124621.
Lundström, T.S., Gustavsson, L.H., Jēkabsons, N., Jakovics, A., 2008. Wetting dynamics in multiscale porous media. Porous pore-doublet model, experiment and theory. AIChE J. 54 (2), 372–380.
Lysyy, M., Liu, N., Solstad, C.M., Fernø, M.A., Ersland, G., 2023. Microfluidic hydrogen storage capacity and residual trapping during cyclic injections: implications for underground storage. Int. J. Hydrogen Energy 48 (80), 31294–31304.
McCollom, T.M., Bach, W., 2009. Thermodynamic constraints on hydrogen generation during serpentinization of ultramafic rocks. Geochim. Cosmochim. Acta 73 (3), 856–875.
McCollom, T.M., Klein, F., Moskowitz, B., Solheid, P., 2022. Experimental serpentinization of iron-rich olivine (hortonolite): implications for hydrogen generation and secondary mineralization on Mars and icy moons. Geochim. Cosmochim. Acta 335, 98–110.
McCollom, T.M., Klein, F., Moskowitz, B., Berquó, T.S., Bach, W., Templeton, A.S., 2020. Hydrogen generation and iron partitioning during experimental serpentinization of an olivine–pyroxene mixture. Geochim. Cosmochim. Acta 282, 55–75.
Mehmani, A., Kelly, S., Torres-Verdín, C., Balhoff, M., 2019. Capillary trapping following imbibition in porous media: microfluidic quantification of the impact of pore-scale surface roughness. Water Resour. Res. 55 (11), 9905–9925.
National Research Council, 1996. The Waste Isolation Pilot Plant: a Potential Solution for the Disposal of Transuranic Waste. National Academies Press.
Niu, B., Al-Menhali, A., Krevor, S.C., 2015. The impact of reservoir conditions on the residual trapping of carbon dioxide in B erea sandstone. Water Resour. Res. 51 (4), 2009–2029.
Osselin, F., Soulaine, C., Fauguerolles, C., Gaucher, E.C., Scaillet, B., Pichavant, M., 2022. Orange hydrogen is the new green. Nat. Geosci. 15 (10), 765–769.
Pan, B., Yin, X., Zhu, W., Yang, Y., Ju, Y., Yuan, Y., Iglauer, S., 2022. Theoretical study of brine secondary imbibition in sandstone reservoirs: implications for H2, CH4, and CO_2 geo-storage. Int. J. Hydrog. Energy 47 (41), 18058–18066.
Porter, M.L., Wildenschild, D., Grant, G., Gerhard, J.I., 2010. Measurement and prediction of the relationship between capillary pressure, saturation, and interfacial area in a NAPL-water-glass bead system. Water Resour. Res. 46 (8).
Roman, S., Abu-Al-Saud, M.O., Tokunaga, T., Wan, J., Kovscek, A.R., Tchelepi, H.A., 2017. Measurements and simulation of liquid films during drainage displacements and snap-off in constricted capillary tubes. J. Colloid Interface Sci. 507, 279–289.
Shams, M., Raeini, A.Q., Blunt, M.J., Bijeljic, B., 2018. A numerical model of two-phase flow at the micro-scale using the volume-of-fluid method. J. Comput. Phys. 357, 159–182.
Suekane, T., Nobuso, T., Hirai, S., Kiyota, M., 2008. Geological storage of carbon dioxide by residual gas and solubility trapping. Int. J. Greenh. Gas Control 2 (1), 58–64.
Thaysen, E.M., Butler, I.B., Hassanpouryouzband, A., Freitas, D., Alvarez-Borges, F., Krevor, S., Edlmann, K., 2023. Pore-scale imaging of hydrogen displacement and trapping in porous media. Int. J. Hydrog. Energy 48 (8), 3091–3106.
Tounsi, H., Rutqvist, J., Hu, M., Wolters, R., 2023. Numerical investigation of heating and cooling-induced damage and brine migration in geologic rock salt: insights from coupled THM modeling of a controlled block scale experiment. Comput. Geotech. 154, 105161.
van Rooijen, W., Hashemi, L., Boon, M., Farajzadeh, R., Hajibeygi, H., 2022. Microfluidics-based analysis of dynamic contact angles relevant for underground hydrogen storage. Adv. Water Resour. 164, 104221.
Wallace, R.L., Cai, Z., Zhang, H., Zhang, K., Guo, C., 2021. Utility-scale subsurface hydrogen storage: UK perspectives and technology. Int. J. Hydrog. Energy 46 (49), 25137–25159.
Wang, J., Yang, Y., Cai, S., Yao, J., Xie, Q., 2023. Pore-scale modelling on hydrogen transport in porous media: implications for hydrogen storage in saline aquifers. Int. J. Hydrog. Energy 48 (37), 13922–13933.
Zamula, Y.S., Batyrshin, E.S., Latypova, R.R., Abramova, O.A., Pityuk, Y.A., 2019. Experimental study of the multiphase flow in a pore doublet model. J. Phys. Conf. Ser. 1421 (1), 012052. , No.
Zgonnik, V., 2020. The occurrence and geoscience of natural hydrogen: a comprehensive review. Earth Sci. Rev. 203, 103140.